Feather-inspired flow control device across flight regimes

IOP Publishing Bioinspir. Biomim. 18 (2023) 066010 https://doi.org/10.1088/1748-3190/acfa4f

Bioinspiration & Biomimetics

OPEN ACCESS

RECEIVED
25 June 2023

REVISED
31 August 2023

ACCEPTED FOR PUBLICATION
15 September 2023

PUBLISHED
4 October 2023

PAPER

Feather-inspired flow control device across flight regimes

Ahmed K Othman[1,*], **Nirmal J Nair**[2], **Andres Goza**[2] and **Aimy Wissa**[1]

[1] Department of Mechanical and Aerospace Engineering, Princeton University, Princeton, NJ 08544, United States of America
[2] Department of Aerospace Engineering, University of Illinois at Urbana-Champaign, Urbana, IL 61801, United States of America
* Author to whom any correspondence should be addressed.

E-mail: ao0951@princeton.edu

Keywords: bio-inspired flow control, avian-inspired flight, feather-inspired device, fluid-structure interaction

Abstract

Bio-inspired flow control strategies can provide a new paradigm of efficiency and adaptability to overcome the operational limitations of traditional flow control. This is particularly useful to small-scale uncrewed aerial vehicles since their mission requirements are rapidly expanding, but they are still limited in terms of agility and adaptability when compared to their biological counterparts, birds. One of the flow control strategies that birds implement is the deployment of covert feathers. In this study, we investigate the performance characteristics and flow physics of torsionally hinged covert-inspired flaps mounted on the suction side of a NACA2414 airfoil across different Reynolds numbers, specifically 200,000 and 1,000. These two Reynolds numbers are representative of different avian flight regimes where covert feathers have been observed to deploy during flight, namely cruising and landing/perching. We performed experiments and simulations where we varied the flap location, the hinge stiffness, and the moment of inertia of the flap to investigate the aerodynamic performance and describe the effects of the structural parameters of the flap on the aerodynamic lift improvements. Results of the study show up to 12% lift improvement post-stall for the flapped cases when compared to the flap-less baseline. The post-stall lift improvement is sensitive to the flap's structural properties and location. For instance, the hinge stiffness controls the mean deflection angle of the flap, which governs the resulting time-averaged lift improvements. The flap moment of inertia, on the other hand, controls the flap dynamics, which in turn controls the flap's lift-enhancing mechanism and how the flap affects the instantaneous lift. By examining the time-averaged and instantaneous lift measurement, we uncover the mechanisms by which the covert-inspired flap improves lift and highlights similarities and differences across Reynolds numbers. This article highlights the feasibility of using covert-inspired flaps as flow control across different flight missions and speeds.

Nomenclature

α	Angle of attack
β	Flap deployment angle
$\overline{\beta}$	Mean flap deployment angle
c	Airfoil chord length
C_l	Coefficient of lift
$\Delta\overline{C}_l$	Percentage change in mean lift relative to baseline airfoil
$\boldsymbol{f}$	Surface stress on body
Fr	Froude number
$\boldsymbol{g}$	Gravitational field
g	Reference acceleration due to gravity
Γ	Set of bodies
Γ_a, Γ_f	Bodies of airfoil and flap
i_β, I_β	Dimensionless and dimensional flap moment of inertia
k_β, K_β	Dimensionless and dimensional stiffness of torsional spring
l_β, L_β	Dimensionless and dimensional chordwise flap location
l_f	Length of the flap
ν	Kinematic viscosity

p, P	Dimensionless and dimensional pressure field
P_∞	Freestream pressure
ρ_f	Fluid density
Re	Reynolds number
St	Strouhal number
t	Time
T	Time period of steady limit cycle oscillations (LCO)
$\boldsymbol{u}$	Fluid velocity
U_∞	Freestream velocity
$\boldsymbol{\chi}, \boldsymbol{\chi}_a, \boldsymbol{\chi}_f$	Lagrangian coordinate of body, airfoil and flap
$\boldsymbol{\chi}_f^0, \boldsymbol{\chi}_f^{cg}$	Flap hinge location and center of gravity
Ω	Flow domain

1. Introduction

Missions for small uncrewed aerial vehicles (sUAVs) are expanding rapidly to meet various application requirements, including search and rescue, cargo transport, surveillance, mapping, and urban planning. Due to this rapid expansion, sUAVs require a flow control technique that can adapt to different mission requirements [5, 13]. In aerodynamics, flow control is defined as the process of favorably altering the flow characteristics to achieve a desired effect; examples include delaying laminar-turbulent transition, mitigating separation, and enhancing mixing. The goals of flow control often involve reducing drag, enhancing lift, or suppressing noise from propulsion systems [15]. flow control strategies may be broadly characterized as either passive or active. Active flow control techniques such as synthetic jets and plasma actuators require actuation and feedback information to adapt to time-varying processes and unexpected or abrupt changes in condition, adding to their volume and power requirements and their design complexity. On the other hand, traditional passive flow control techniques, such as distributed roughness, require no actuation or feedback. However, these approaches are unable to respond to abrupt flow changes [14]. A passive yet adaptive flow control technique has the potential to enable sUAV designs capable of the broad range of mission portfolios while adhering to the requisite power availability and volume constraints.

Birds that operate at a similar Reynolds number (Re) to sUAVs are often observed to be mission adaptable. The same bird can perch, glide, and maneuver during flight with superior agility compared to sUAVs. This superiority is enabled by multiple flow control systems ranging from active global wing articulation to multiple passive and active feather systems on both the upper and lower sides of the wing [12, 25]. One of those feather systems, which we focus on in this article, is the covert feathers (cf figure 1(a)) that deploy during gust and high angle-of-attack maneuvers such as perching, takeoff, and landing. Biological studies on covert feathers suggest they act as passive lift-enhancing flow control devices [7, 9]. Carruthers *et al* [9] analyzed flight videos of a steppe eagle and noticed that during high-angle-of-attack maneuvers, such as landing, take-off, and perching, the lesser covert feathers on the pressure side (i.e. lower surface) of the wing deploy, while during gust conditions the greater coverts deploy on the suction side (i.e. upper surface) of the wing.

Motivated by these observations in nature, bio-inspired studies have investigated covert-inspired flaps affixed to engineered wings at a wide range of flow conditions and Reynolds numbers. These studies included different structural and mobility forms of the flaps to improve aerodynamic performance. Structural forms include rigid metal flaps, feathered flaps, and elastic hair-like flaps, while mobility forms involve flaps affixed via a hinge to the wing, either in a fixed static position or via a hinge that enables adaptive deployment and response to the flow [1, 6, 8, 11, 20, 28, 31]. In this wide range of settings, the covert-inspired flaps were found to provide benefits as a post-stall lift enhancement device. At intermediate Reynolds numbers relevant to bird cruising flight, $\mathrm{Re} = O(10^5)$, studies demonstrated that static flaps fixed at a certain angle can improve post-stall lift by as much as 23% [11, 20]. On the other hand, freely hinged flaps at the same Reynolds number range were shown to provide lift improvements up to 18% as well as delay the stall angle of attack [6, 19, 20]. At lower Reynolds numbers, $\mathrm{Re} = O(10^3)$, which is more relevant for landing and perching maneuvers, studies show that covert-inspired flaps can improve lift up to almost 10% for a rigid static flap and 13.5% for a freely moving flap [18]. With a few exceptions [22, 23, 28], the focus of these studies has been on flaps that are either static or fully free to rotate (i.e. with a zero or approximately zero hinge stiffness). Nair *et al* [22] looked at the effect of a nonzero stiffness hinge at a Reynolds number of 1,000 and found lift improvements of up to 23%, with a strong dependence of lift improvements on the hinge stiffness and flap inertia. However, to the authors' awareness, no attempts have assessed the effect of torsionally hinged covert-inspired flaps across Reynolds numbers.

Thus, questions remain about the role of covert feathers and covert-inspired flap structural properties in post-stall flight conditions across Reynolds numbers. In particular, biological studies suggest that the deflection of feathers during flight is dependent upon the mass and flexural stiffness of the rachis (cf figure 1(b)), which is the main feather shaft [3]. Moreover, it was shown in a study by Wang *et al* that different bird species have different degrees of flexibility in their feathers, with larger birds having more flexible feathers than their smaller counterparts [32]. Thus, there is a need to study the effect of feather stiffness and mass on the deployment of the coverts during flight and the corresponding aerodynamics that

(a) Rows of upper wing coverts on a heron wing [26] **(b)** Structure of heron's upper and under wing coverts [30]

Figure 1. Different rows of covert feathers on the upper surface of a heron wing (left), and the upper and under wing covert feathers structure (right). (Photo Credit: (a) Adapted with permission from [26]. This image has been obtained by the author(s) from the Pixabay website where it was made available under the Pixabay License. It is included within this article on that basis https://pixabay.com/photos/heron-in-flight-flying-heron-heron-4573818/. (b) Reproduced with permission from [30]).

results from such deployment. Such studies should also clarify the physical mechanisms that allow lift improvements, especially across different Reynolds numbers, which can be representative of different flight stages, such as cruise and perching.

In this article, we implement a more representative analogy of the covert feathers, where the covert-inspired flaps are torsionally hinged to a lifting surface. We focus on analyzing the effects of the hinge stiffness and the flap mass. More specifically, using a systematic experimental and high-fidelity numerical parametric study, we answer the following questions:

(Q1) Are the aerodynamic benefits of the torsionally hinged covert-inspired flaps transferable across different Reynolds numbers, representative of different flight regimes?
(Q2) What are the effects of the hinge stiffness and the flap mass on the aerodynamic benefits across the Reynolds number regimes?
(Q3) How do the physics of this fluid-structure interaction system change from low Reynolds numbers associated with landing and takeoff maneuvers compared to the higher Reynolds numbers more relevant to gliding?

2. Methods

2.1. Problem overview and parameters

In this study, the covert feathers are modeled as passively deployable, torsionally hinged rigid flap on the upper surface of a stationary NACA2414 airfoil as shown in figure 2. This airfoil was selected because it has been well characterized in wind tunnel tests across various Reynolds numbers and it is suitable for small-scale UAVs. The chord-based Reynolds number is set to $\mathrm{Re} = 200,000$ for the experiments and $\mathrm{Re} = 1,000$ for the numerical simulations. To indicate differences and similarities in the baseline flow (without a flap) across Reynolds number, we show in figure 3 the time-averaged lift ($\overline{C_l}$) versus angle of attack (α). For $\mathrm{Re} = 200,000$, $\alpha = 20^\circ$ clearly corresponds to a post-stall angle of attack due to the sharp decline in $\overline{C_l}$ after $\alpha = 16^\circ$. On the other hand, for $\mathrm{Re} = 1,000$, the stall angle is not discernible since the lift continues to increase with increasing α. Therefore, to identify the stall angle, we have also shown the amplitude of fluctuations in C_l denoted by the gray shaded region. These (limit cycle) oscillations (LSO) occur due to flow separation on the upper surface of the airfoil and the ensuing periodic vortex shedding. Notable separation-induced fluctuations start from $\alpha = 10^\circ$ with significant fluctuations at 20°. Therefore, $\alpha = 20^\circ$ corresponds to a post-stall angle for $\mathrm{Re} = 1,000$ as well and is the angle of attack chosen for this study. We consider the use of validated simulation tools in conjunction with carefully conducted experiments to explore the effect of Reynolds number on the fluid-structure interaction dynamics of this flap system. The solver has been validated in Goza and Colonius [17], Goza *et al* [18], Nair and Goza [21], and offers a high-fidelity framework to compute the FSI dynamics at low Reynolds numbers, relevant to perching, that would be challenging to access experimentally because of the low flow speeds that would be required. By contrast, experiments are performed at high Reynolds numbers where prohibitively costly simulations would be required, with appropriate treatment of three-dimensional effects and turbulence models for unresolved regions near the body and in the wake.

For the experiments and the simulations, the chord length of the airfoil is denoted by c, and the length of the flap is fixed at $0.15c$. The $\mathrm{Re} = 1,000$ case

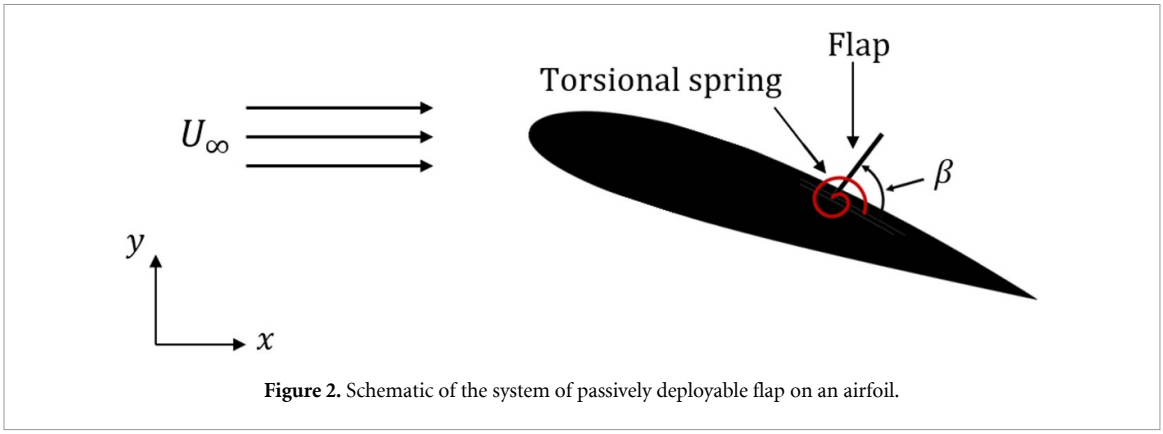

Figure 2. Schematic of the system of passively deployable flap on an airfoil.

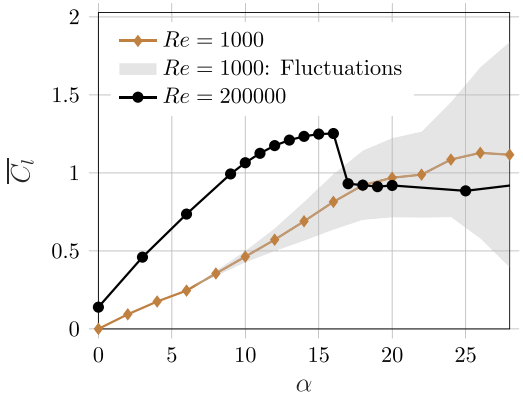

Figure 3. $\overline{C_l}$ versus α for Re $= 200,000$ and Re $= 1,000$. Gray shaded region denotes the peak-to-peak amplitude in the time-varying fluctuations in C_l at Re $= 1,000$.

is simulated under gravity with Froude number (Fr $= U_\infty/\sqrt{gc}$) of 23.96 which matches the experiment. The varying flap and hinge parameters in this study are the moment of inertia of the flap, I_β, the stiffness of the torsional spring representing the hinge, K_β, and the chordwise distance of the flap from the leading edge, L_β. These parameters are non-dimensionalized as,

$$i_\beta = \frac{I_\beta}{\rho_f c^4}, \qquad k_\beta = \frac{K_\beta}{\rho_f {U_\infty}^2 c^2}, \qquad l_\beta = \frac{L_\beta}{c}. \quad (1)$$

Here, the reference length scale is the airfoil chord c, the velocity scale is the freestream velocity U_∞, and the density scale is the fluid density ρ_f. i_β, k_β and l_β are the non-dimensional counterparts of I_β, K_β and L_β. In the manuscript, the parameter l_β is reported as a percentage of chord length from the leading edge. The length and locations of the flap were specified based on several design parameters in the literature [8, 11, 21, 31]. All the fixed and varying parameters for the numerical simulations and experiments are reported in table 1. From table 1, it is clear that the only key different parameter is the Reynolds number, allowing us to investigate its effects on the flap dynamics and the flap-induced aerodynamic improvements.

2.2. Experimental setup

2.2.1. Wind-tunnel setup

The experiments are carried out in the constant pressure, closed section, open-loop wind tunnel located in Talbot Laboratory at the University of Illinois at Urbana-Champaign. The wing is horizontally mounted in the first test section closest to the inlet since it has the lowest turbulence level. The dimensions of the test section are 90 cm in width and 45 cm in height. One end of the wing section is mounted to the side of the wind tunnel, while the other side is connected to a splitter plate to ensure 2D test conditions as shown in figure 4(a). The splitter plate reduces the test section width to 28 cm while maintaining a constant height of 45 cm, thereby mitigating the impact of the upper and lower section walls on the streamlines, as discussed in Duan and Wissa [11]. The splitter plate is 45 cm in height, covering the whole test section height, and 91.4 cm in width with a 1.2 cm thickness. Velocity corrections are performed to account for the splitter plate effect using the methods in Giguére and Selig [16]. The wing section is connected to the splitter plate on one end with a paper-thin gap to avoid unintended reaction forces. An ATI Gamma 6-axis force/torque transducer is used to measure the forces on the wing, with a resolution of 1/60 N and a range of 0–32 N. A B48 Velmex rotary table with a stepper motor controls the angle of attack with a precision of 0.012°. The lift and drag are calculated from the measured forces, sampled at 1 kHz for 5 s, and the angle of attack is used to rotate them to the wind frame of reference. Lift values were compared to the airfoil database, and the results show good agreement with the two-dimensional airfoil [29]. The experiments are carried out at a free stream velocity of 26 m s^{-1} for an airfoil with a 0.12 m chord. Data acquisition starts after 5 s from setting the desired angle of attack to ensure steady-state conditions. Then force data is collected for 5 s or 1083 convective time units (tU_∞/c).

The freestream velocity is measured using an Omega volume flow anemometer placed upstream of the wing, between the splitter plate and the wind tunnel wall. The anemometer has a resolution of

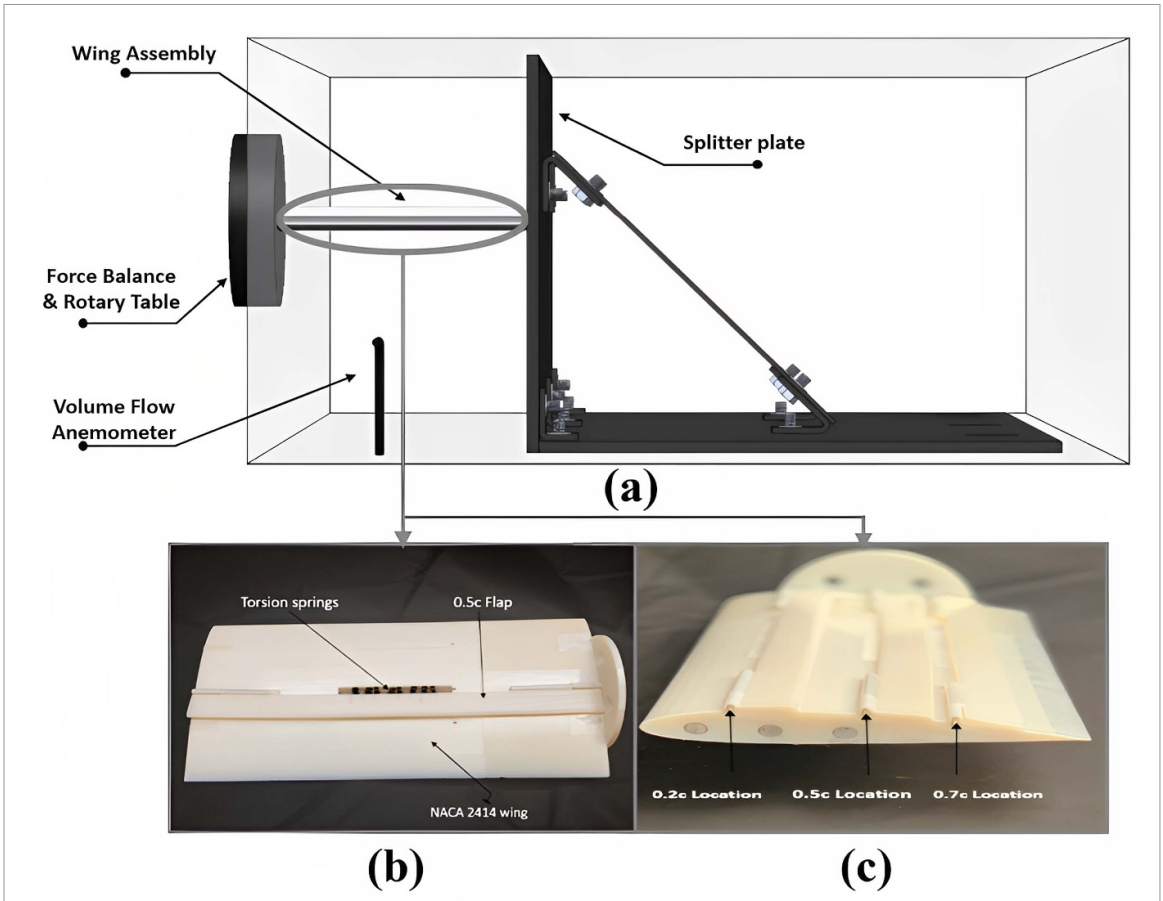

Figure 4. Schematic of wind tunnel setup (a) and wing assembly (b & c).

Table 1. List of fixed and varying parameters for experiments and numerical simulations.

	Parameters	Values	
Fixed parameters	Re	Experimental	Numerical
		200,000	1,000
	Airfoil	NACA2414	
	Angle of attack	20°	
	Flap length	0.15	
	Fr	23.96	
Varying parameters	Flap location (l_β)	{20, 50, 70}%	
	Stiffness of hinge (k_β)	{0.0001, 0.0005, 0.001}	
	Flap moment of inertia (i_β)	{0.0012, 0.012}	

0.01 m s^{-1} and an accuracy of $\pm 1.0\%$ of reading. Furthermore, corrections are made in the post-processing code to account for solid and wake blockage. [2, 4, 29]. The free stream velocity during the experiments was 26 m s^{-1}, which corresponds to $Re = 200,000$.

The flap dynamics, including its flapping frequency and deflection angles, are captured using Vision Research Phantom Miro eX4 Color high-speed camera at 600 fps. The flap recordings were post-processed using the ProAnalyst Motion Analysis Software.

2.2.2. Wing design

The wing section is made from VeroWhite material using an objet 260 connex3 3D printer. The hinge is designed with two detachable circular hinges with a diameter of 2 mm placed on each side of the wing that connects to their corresponding circular hinges on the flap through a metal rod. To control the stiffness of the hinge, torsion springs are inserted around the metal rod, as illustrated in figure 4(b). Each torsion spring has an outer diameter of 5.3 mm and torsional stiffness of 1.5×10^{-3} N.m rad^{-1}. The hinge stiffness imposes a torque that keeps the flap

tangent to the airfoil suction surface or closed ($\overline{\beta} = 0$) with no wind. When the fluid-induced forces exceed the restoring force of the hinge and the flap's inertia, the flap deploys ($\overline{\beta} > 0$) and starts oscillating around its mean deflection angle. By attaching one, four, or eight springs in parallel, dimensional torsional stiffness values of 1.5×10^{-3}, 6.0×10^{-3}, and 12×10^{-3} N.m rad^{-1} are obtained, respectively. These dimensional stiffness values correspond to the non-dimensional stiffness values reported in table 1. Two different materials with distinct densities are utilized to modify the flap's inertia and mass, namely VeroWhite and Mylar with a thickness of 2 mm and 0.2 mm, respectively. These materials result in the following dimensional inertia values: 8.53×10^{-7} and 8.64×10^{-8} kg m^2, respectively, also listed in table 1 in their non-dimensional form.

The wing section design allows for adjusting the flap location. Figure 4(c) shows the wing section with three flaps located at 0.2c, 0.5c, and 0.7c. During the experiments, only one flap was tested. Meanwhile, the hinge locations for the other flaps were covered by 3D-printed adaptors to maintain the airfoil profile. For example, figure 4(b) shows the wing section with a single flap placed at 0.5c, with the adaptors covering the remaining two flap location slots

2.3. Numerical methodology

The strongly-coupled projection-based immersed boundary method of Nair and Goza [21] is utilized to perform the numerical simulations in this work. This method has been successfully applied and validated on problems involving torsionally mounted flaps [21–23] and utilizes a framework that extends the original projection-based fluid-structure interaction method of Goza and Colonius [17] to more general bodies. The method numerically solves the following dimensionless governing equations,

$$\frac{\partial \boldsymbol{u}}{\partial t} + \boldsymbol{u}\cdot\nabla\boldsymbol{u} = -\nabla p + \frac{1}{Re}\nabla^2\boldsymbol{u} + \int_\Gamma \boldsymbol{f}(\boldsymbol{\chi}(s,t))\,\delta\left(\boldsymbol{\chi}(s,t)-\boldsymbol{x}\right)\mathrm{d}s + \frac{1}{\mathrm{Fr}^2}\boldsymbol{g} \tag{2}$$

$$\nabla\cdot\boldsymbol{u} = 0 \tag{3}$$

$$i_\beta\frac{\partial^2\beta}{\partial t^2} + k_\beta\beta = -\int_{\Gamma_f}\left(\boldsymbol{\chi}_f - \boldsymbol{\chi}_f^0\right)\times\boldsymbol{f}(\boldsymbol{\chi}_f)\,\mathrm{d}\boldsymbol{\chi}_f + \frac{3i_\beta}{l_f^2\mathrm{Fr}^2}\left(\boldsymbol{\chi}_f^{cg} - \boldsymbol{\chi}_f^0\right)\times\boldsymbol{g} \tag{4}$$

$$\int_\Omega \boldsymbol{u}(\boldsymbol{x})\,\delta\left(\boldsymbol{x}-\boldsymbol{\chi}_a\right)\mathrm{d}\boldsymbol{x} = 0 \tag{5}$$

$$\int_\Omega \boldsymbol{u}(\boldsymbol{x})\,\delta\left(\boldsymbol{x}-\boldsymbol{\chi}_f\right)\mathrm{d}\boldsymbol{x} = \frac{\partial\beta}{\partial t}\hat{\boldsymbol{e}}^i\times\left(\boldsymbol{\chi}_f-\boldsymbol{\chi}_f^0\right). \tag{6}$$

The immersed boundary method uses two separate grids for spatial discretization: one fixed and the other moving in order to represent the flow domain and the surface of the body, respectively. Accordingly, in this work, a fixed Eulerian coordinate is used for the fluid domain Ω, and a moving Lagrangian coordinate is used for the body surface (airfoil and flaps) Γ. $\boldsymbol{x}$ denotes the Eulerian coordinate representing the position in Ω, and $\boldsymbol{\chi}(s,t)$ denotes the Lagrangian coordinate attached to the bodies (airfoil and flap) in Γ, in which s is used to parameterize along the surface.

The variables, $\boldsymbol{x}$, $\boldsymbol{\chi}$, and s are all nondimensionalized by the airfoil chord c. Velocity $\boldsymbol{u}$ is nondimensionalized by the freestream velocity U_∞, and time t is nondimensionalized by c/U_∞. Moreover, pressure p and surface stress imposed on the fluid by the body $\boldsymbol{f}$, and are nondimensionalized by $\rho_f {U_\infty}^2$, where ρ_f is the fluid density, and $\boldsymbol{g}$ is the non-dimensional gravitational field using a reference g. Equation (4) shows the rotational equation of motion for the torsionally-hinged flap Γ_f, where $\boldsymbol{\chi}_f$ denotes the Lagrangian coordinate of Γ_f. In equation (4), the left-hand side shows the inertial and stiffness terms. While on the right-hand side, the first term corresponds to the torque about the hinge, $\boldsymbol{\chi}_f^0$, resulting from the surface stress exerted on the flap by the surrounding fluid, and the second term corresponds to the torque about $\boldsymbol{\chi}_f^0$ due to the gravitational force acting at the flap's center of gravity $\boldsymbol{\chi}_f^{cg}$. It should be noted that the mass of the flap is incorporated in this term using the flap's moment of inertia around the hinge. Equations (5) and (6) show the no-slip boundary condition on the airfoil and flap, respectively. In these equations, $\hat{\boldsymbol{e}}^i$ is a unit vector indicating the direction of the flap's angular velocity, and $\boldsymbol{\chi}_a$ is the Lagrangian coordinate of the airfoil. These no-slip constraints provide closure to the governing equations in order to solve for the surface stress term $\boldsymbol{f}(\boldsymbol{\chi})$ that enforces the boundary condition on the respective bodies.

The flow equations (2) and (3) are rewritten in a streamfunction-vorticity formulation and spatially discretized using the conventional second-order finite difference method. Equation (2) is temporally discretized using an Adams-Bashforth scheme for the nonlinear term and a Crank-Nicolson method for the diffusive term. The flap's equation of motion, equation (4), is temporally discretized using an implicit Newmark scheme. The boundary constraints (5) and (6) and the surface stress term in equation (2) are implicitly treated at the current time step to ensure method stability for a broad range of flap inertias and stiffness. After full discretization, the resulting system of equations is solved by performing a block-LU decomposition and iterating the fluid-structure interaction terms using Newton's method until convergence is achieved for the flap deflection angle. To enforce the far-field Dirichlet boundary conditions of zero vorticity, a multi-domain approach is

incorporated for solving the flow equations. In this approach, the entire domain is partitioned using a hierarchy of grids of increasing coarseness extending to the far field (see [10] for details).

In this work, the spatial grid and time step sizes are set to $\Delta x/c = 0.00349$ and $\Delta t/(c/U_\infty) = 0.0004375$, respectively. This setup is based on the previously conducted grid-convergence study in Nair and Goza [21] for the same passively deployable airfoil-flap system, but with a NACA0012 airfoil. According to Goza and Colonius [17], the immersed boundary spacing is set to be twice the spacing of the finest flow grid. The convergence criteria for the deflection angle is $\|\Delta\beta\|_\infty \leqslant 10^{-7}$. For the multi-domain approach used for the far-field Dirichlet boundary conditions, five grids of increasing coarseness are implemented, where the finest grid level is $[-0.5, 2.5]c \times [-1.5, 1.5]c$ and the coarsest grid level is $[-23, 25]c \times [-24, 24]c$. Initially, the flap is positioned at an angle of 5° relative to the airfoil surface; this angle serves as the reference undeformed (zero stress) deflection angle. As the flow undergoes vortex shedding at a high angle of attack of 20°, the passive deployment of the flap occurs, leading to its interaction with the flow.

3. Results

3.1. Overview

Figure 5(a) shows the time-averaged lift coefficient, $\overline{C_l}$, as a function of the airfoil angle of attack, α, for all the configurations with the covert-inspired flap compared to the baseline, or the flap-less configuration, at $\mathrm{Re} = 200,000$. In the figure, the lift force is averaged for all flap locations, hinge stiffness, and flap inertia. The average value is indicated by the solid line, while the shaded region indicates the range of time-averaged lift values measured for all flap configurations. The mean lift values results confirm findings of prior studies that covert-inspired flaps are post-stall lift enhancement devices [1, 6, 11, 20, 22, 24, 28]. On average, the flap improves lift at post-stall angles of attack ($\alpha > 16°$), while at pre-stall angles ($\alpha < 16°$), the flap is either detrimental or has no effect on lift, depending on the flap parameters. At post-stall conditions, the flap has either a favorable or negligible effect on drag, resulting in overall aerodynamic efficiency improvements. Some representative cases of time-averaged lift coefficient, $\overline{C_l}$ and drag coefficient $\overline{C_d}$ as a function of the airfoil angle of attack, α are shown in the appendix section along with $\overline{C_l}$ vs $\overline{C_d}$ plot.

For the remainder of the paper, we focus on lift results as during post-stall conditions, where lift losses are the most limiting to the operational envelopes of sUAVS. More specifically, we will focus on the flap deployment behavior and resulting lift forces in the post-stall regime, namely, $\alpha = 20°$ at $\mathrm{Re} = 200,000$ and $\mathrm{Re} = 1,000$ representative of flight and perching or landing maneuvers speeds, respectively. At this post-stall α, the average lift is sensitive to the flap location and structural properties, as indicated by the shaded region in figure 5(a). Even at a particular flap location (cf figure 5(c)), the time-averaged lift is sensitive to the hinge stiffness and the flap inertia for the $\mathrm{Re} = 200,000$ experiments. The lift's sensitivity to the flap structural properties is also observed at $\mathrm{Re} = 1,000$, as shown in figure 5(b). Comparing, figures 5(b) and (c), we observe similarities (particularly for low inertia and high stiffness values) and differences in the lift improvements across the Reynolds numbers.

We break our analysis into two stages to quantify and explain these similarities and differences. To answer the questions related to the aerodynamic benefits of the flap across Reynolds number and the effect of the flap parameters on such benefits (Q1 and Q2), we will first focus on the time-averaged lift force and the corresponding mean flap deflection for the low inertia flaps where the benefits are more pronounced and the flaps deploy at both Reynolds numbers. We will then examine the dynamics of the flap deflection and lift force to identify the fluid-structure interaction mechanisms and their dependency on the Reynolds number and the flap parameters (Q3).

3.2. Time-averaged results

At both Reynolds numbers, the low inertia flap improved lift more than the high inertia flap, as shown in figures 5(b) and (c). We, therefore, focus our results on this low inertia regime. Figure 6 shows the effect of the flap location and hinge stiffness on the mean deflection angle $\overline{\beta}$ and the mean lift improvement $\Delta\overline{C_l}$ for the low inertia flaps at $\alpha = 20°$. In these plots, $\Delta\overline{C_l}$ (%) is calculated relative to the baseline or the flap-less case. For the 70% location (figure 6(c)) at both Reynolds numbers, as the k_β increases, the mean flap deployment angle decreases due to the increasing restoring torque imposed by the torsional spring. Moreover, as k_β is increased, the $\Delta\overline{C_l}$ increases at the 70% location. Here, we note that the case of $k_\beta = 0.001$ at 70% location provides the most lift improvement of any case at this angle of attack at both Reynolds numbers regimes. A different trend is observed at the 20% location, shown in figure 6(a): the mean deflection angle stays almost constant for both Reynolds numbers around 20°, and there is a minimal commensurate effect on the mean lift of $\Delta\overline{C_l} \approx 2\% - 3\%$ for both Reynolds number cases. The little change in mean lift suggests that, at the 20% location, the flap cannot significantly modify the separation-induced reverse flow along the suction surface. Similarly, the negligible change in mean deflection angle suggests a large region of fully separated flow near the leading edge. Since the flow is fully separated at this angle of attack, the airfoil suction peak collapses, and the C_P curve flattens. The higher pressure and lack of pressure differential along

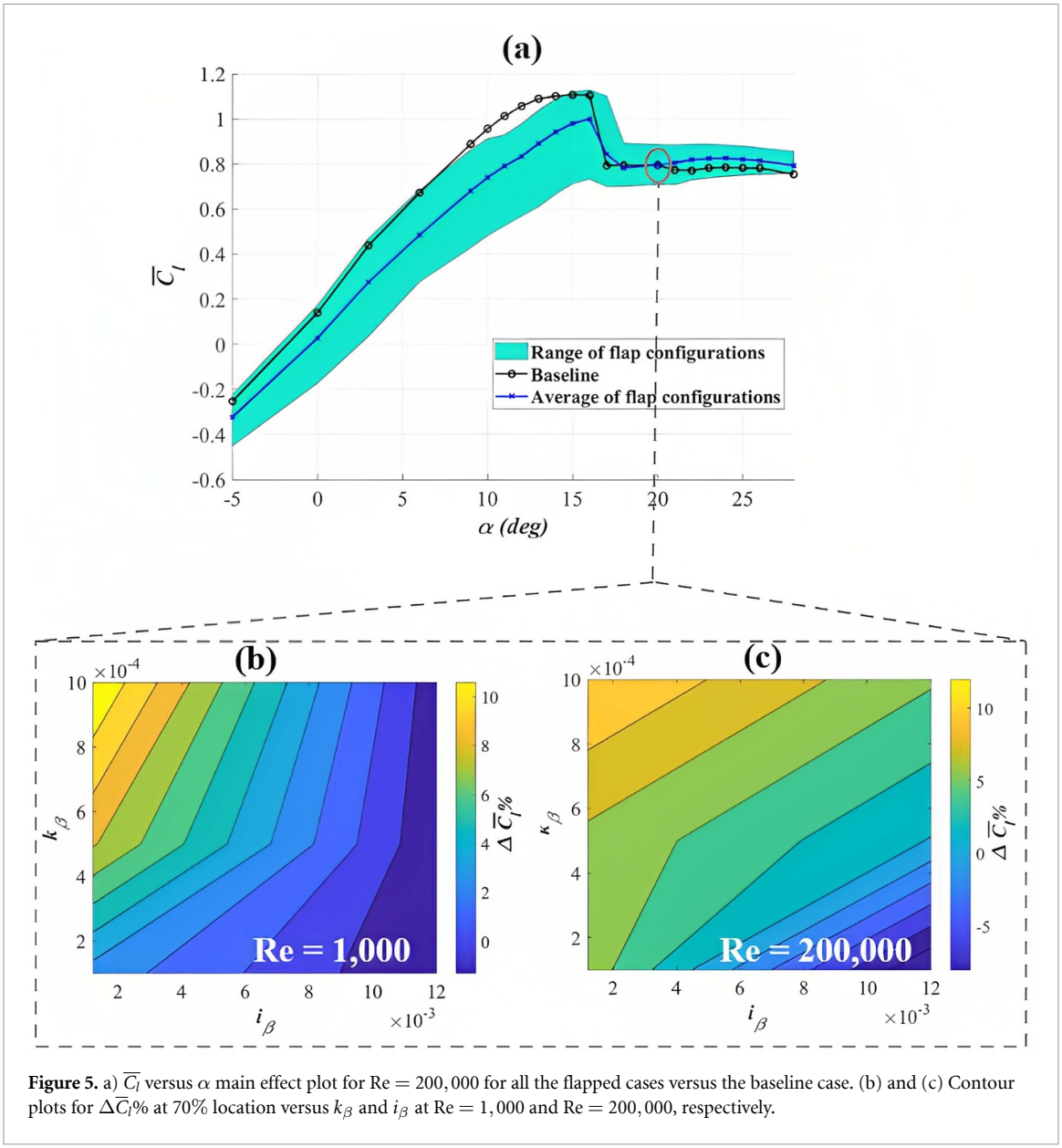

Figure 5. a) $\overline{C}_l$ versus α main effect plot for Re = 200,000 for all the flapped cases versus the baseline case. (b) and (c) Contour plots for $\Delta\overline{C}_l$% at 70% location versus k_β and i_β at Re = 1,000 and Re = 200,000, respectively.

the suction surface at this α prevent the flap from deploying further even as the stiffness is decreased, rendering the flaps ineffective at modulating lift at this location. The inability of the flap to modulate separation near the leading edge or block reverse flow from the trailing edge is apparent in the time average lift (cf figure 6(a)), where there are minimal mean lift changes at this location compared to the baseline. The results from figures 6(a) and (c) highlight that the mean lift changes depend on the mean deflection angle $\overline{\beta}$, set by the combined effect of the aerodynamic forces, restoring force due to k_β, and gravitational forces. Thus, for a given flap inertia and flight conditions, the time-averaged $\Delta\overline{C}_l$ can be tuned via the hinge stiffness and the sensitivity of the time-averaged $\Delta\overline{C}_l$ to changes in the hinge stiffness can be tailored via the flap location.

In contrast to the similar trends across Reynolds numbers observed at the 70% and 20% locations, significant differences are observed across Reynolds numbers at the 50% location. More specifically, no lift benefits are attained at Re = 1,000, while experiments at Re = 200,000 yield $\Delta\overline{C}_l \approx 3\%$ (cf figure 6(b)). This difference is because the flap in the low Reynolds number case does not deploy, as shown by the $\overline{\beta} = 0$ (cf figure 6(b)), whereas considerable $\overline{\beta}$ is observed for the higher Reynolds number experiments. Reynolds number is the ratio of inertial flow effects to viscous effects. Thus, at the higher Reynolds number, one expects the larger flow momentum to yield a greater propensity to overcome the adverse pressure gradient associated with the relatively large angle of attack. As such, the separation location is likely further downstream for the higher Reynolds number compared to the low Reynolds number case. At the lower Reynolds number, the 50% location could be further downstream of the separation location, suggesting that there are few opportunities for the flap to interact with the upstream flow because the shear layer has already separated in this region.

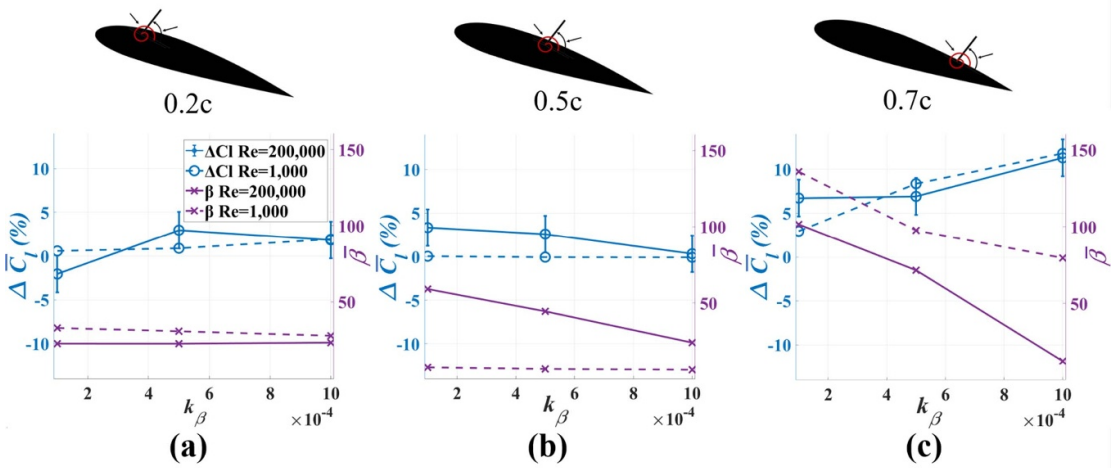

Figure 6. Results of varying the hinge stiffnes of the low inertia flap mounted at (a) 20%, (b) 50%, and (c) 70% chord locations at $\alpha = 20°$. The lift improvement $\Delta\overline{C}_l$ of the airfoil as compared to the baseline flap-less case is plotted in blue, and the mean flap deflection $\overline{\beta}$ is plotted in purple for both Reynolds number cases.

By contrast, at the higher Reynolds number, the flap is probably closer to the shear layer, providing both a broader set of unsteady dynamics from the shear layer that trigger flap motion and a greater ability for the flap to modulate this shear-layer behavior. This outcome suggests that a possible follow-up study of this system as a function of Reynolds number might consider scaled angles of attack to account for the changing impact of the adverse pressure gradient for the different magnitudes of flow momentum.

3.3. Instantaneous results

The third question (Q3) is related to the physics that enables the lift benefits shown in the time-averaged results. We will answer this question by examining the flap dynamics and their interaction with the vortex-shedding to understand the fluid-structure interaction mechanisms by which the flap affects the lift dynamics. Figure 7 shows the amplitude of the flap oscillations, relative to the mean deflection angle $\overline{\beta}$, for the low inertia flaps (purple) and the high inertia flaps (red) for both Reynolds numbers and at the three tested flap locations for the highest stiffness case. The highest stiffness value is chosen for this analysis because it yields significant mean lift improvements across all flap locations; cf figure 6. The results show the low inertia flaps' oscillations are more pronounced ($O(1°)$) compared to the high inertia flaps ($O(0.1°)$). Thus, the low inertia flap deflections may be described as dynamic. In contrast, the high inertia flap deflections are referred to as quasi-static as they are similar to the behavior observed for static flaps studied in Duan and Wissa [11]. The different flap deflection behaviors suggest that while both flaps can improve lift, especially at the high Reynolds number case, as shown in figure 5(c), examining the lift time-varying dynamics is critical to understanding the improvements to the mean quantities.

3.3.1. The lift dyamics of the quasi-static, high inertia flaps

Figures 8(a) and (b) show $C_l(t)$ for the configuration with the most lift improvements of the high inertia flap ($i_\beta = 0.012, k_\beta = 0.001$) for both Reynolds numbers at 70% location. In these plots, time in the x-axis is non-dimensionalized as convection time, normalized using the freestream velocity (U_∞) and chord length (c). For each of these temporal plots in the top row, the bottom row shows the corresponding power spectral density as a function of the Strouhal number defined as $St = fc\sin(\alpha)/U_\infty$, where f is the dimensional frequency in rad/sec, and $c\sin(\alpha)$ is the projected chord length normal to the flow direction (figures 8(c) and (d)).

The high inertia flap does not deploy for the low Reynolds number case and therefore has a negligible effect on the lift measurements; cf figure 8(b). On the other hand, for the high Reynolds number case (figure 8(a)), where the flap deploys, the mean of the lift signal increases by roughly 6%, and the lift fluctuations decrease compared to the baseline. This decrease in lift oscillations is also evident in the power spectral density of C_l, figure 8(c) where the flap reduces the peak amplitude at $St \approx 0.27$. The $St \approx 0.27$ peak is within the range of classic bluff-body shedding behavior [27]. Thus, such reduction in the peak amplitude suggests that the lift improvement mechanism for the high inertia flap relies on preventing the interaction between the flow structures upstream and downstream, resulting in lift oscillation reductions and a pressure dam effect, as previously mentioned in [11, 20] for static flaps.

3.3.2. The lift dyamics of the dynamic, low inertia flaps

Similar to figure 8, figures 9(a) and (b) show $C_l(t)$ signal for the case that produces the best lift improvement for the low inertia flap ($i_\beta = 0.0012$,

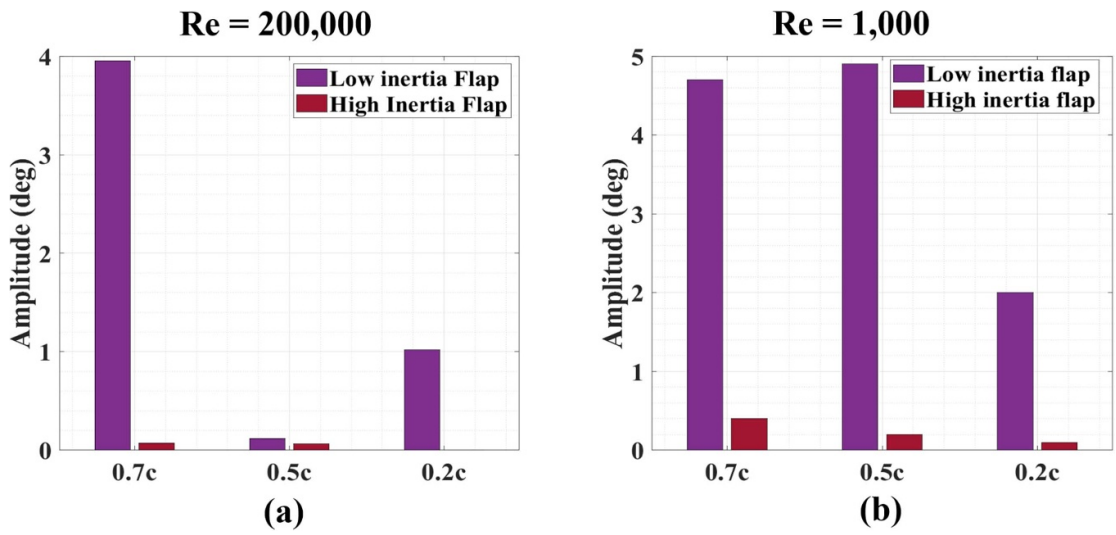

Figure 7. Amplitude from the mean deflection angle for both low and high inertia flaps at (a) Re = 200,000 (b) Re = 1,000.

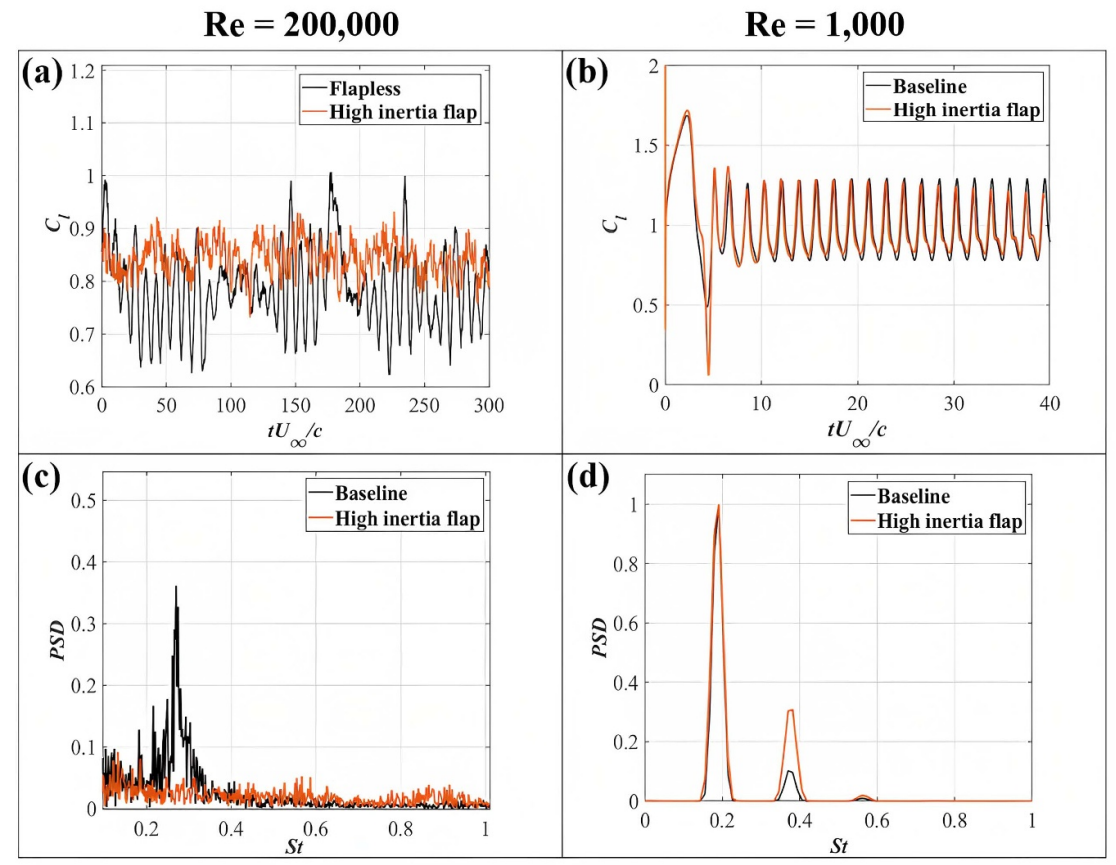

Figure 8. Plots of lift coefficient, C_l, for the flap-less case and the case of high inertia flap located at 70%, $k_\beta = 0.001$ at (a) Re = 200,000 (b) Re = 1,000. Power spectral density (PSD) of the lift signal for the flap-less case and the high inertia flap located at 70%, $k_\beta = 0.001$ at (c) Re = 200,000 (d) Re = 1,000.

$k_\beta = 0.001$) for both Reynolds number at the 70% location. Several differences are observed between the low and high inertia flaps. First, the mean of the lift signal increases at both Reynolds numbers, as opposed to just the higher Reynolds number, which was the case for the high inertia flap. Second, unlike the high inertia flap, the lift fluctuations from the mean of the low inertia flap configuration remain within the same order of magnitude as the baseline configuration. Third, figures 9(c) and (d) show that the dominant peaks in power spectral density, which occur at $St \approx 0.20$ and $St \approx 0.27$ for Re = 1,000 and

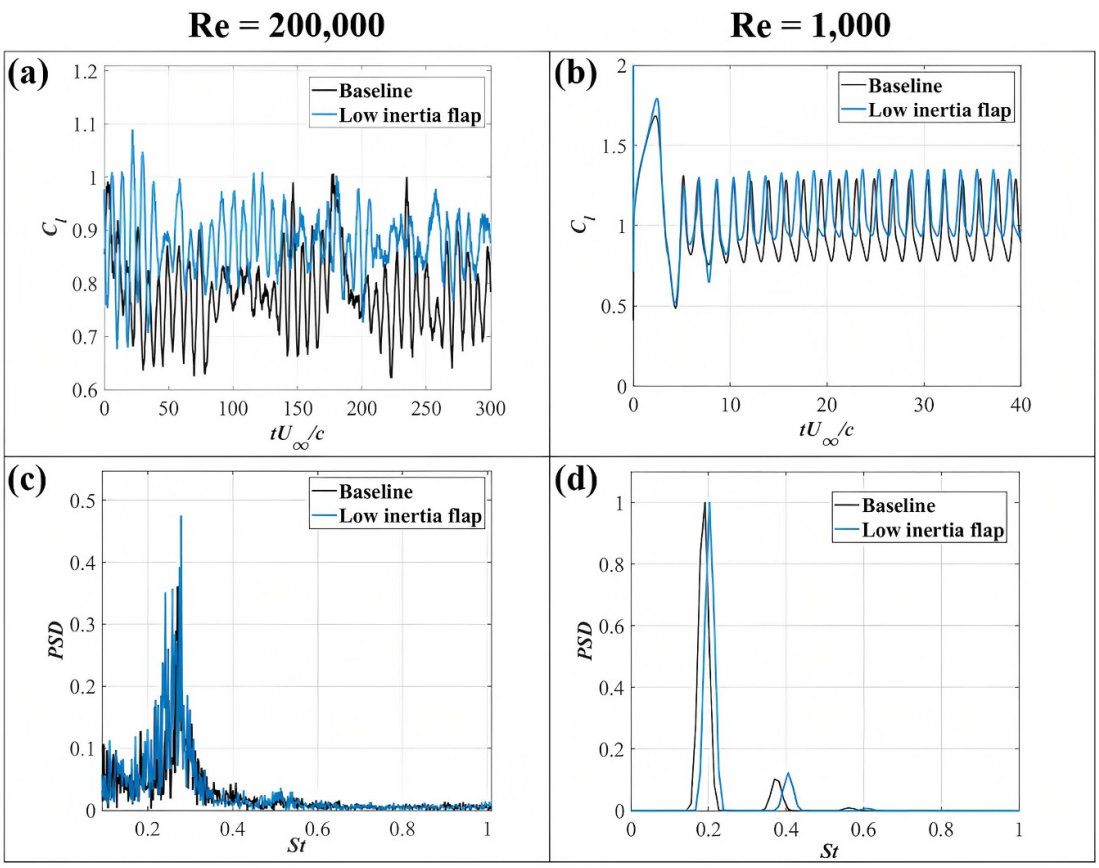

Figure 9. Plots of lift coefficient, C_l, for the flap-less case and the case of low inertia flap located at 70%, $k_\beta = 0.001$ at (a) Re = 200,000 (b) Re = 1,000. Power spectral density (PSD) of the lift signal in for the flap-less case and the low inertia flap located at 70%, $k_\beta = 0.001$ at (c) Re = 200,000 (d) Re = 1,000.

200,000, respectively, are still observed for the low inertia and baseline configuration. Since these *St* numbers are within the range of vortex-shedding frequencies associated with the bluff projected body of the airfoil on the flow, the fact that the low inertia flaps maintain the lift peak and its primary frequency for both Reynolds numbers indicates that the lift improvement mechanism of the low inertia flaps relies on the synchrony between shedding dynamics and flap motion that beneficially modify the lift signature. Finally, the low inertia, dynamic flap lift improvements are superior to those of the high inertia, quasi-static case, indicating that the interplay between the significant flap motion and vortex shedding is critical to maximizing mean lift improvements.

The lift improvement mechanism for the low inertia flap can be visualized by examining the flow field. More specifically, we analyze the lift-enhancing flow structures that are modulated by the dynamics of the low inertia flap at Re = 1,000. Figures 10 and 11 show the vorticity contours with superimposed streamlines in one time period of the lift dynamics in the limit-cycle oscillation (LCO) regime for the maximum lift improvement configuration of $i_\beta = 0.0012$, $k_\beta = 0.001$ at 70% location and the baseline flap-less configuration, respectively. This limit-cycle behavior is associated with periodic vortex shedding from the leading and trailing edges of the airfoil (cf figures 10 and 11). Here, a lift cycle is defined between two consecutive peaks of C_l. The periodic formation, shedding, and interaction of the leading (LEV) and trailing (TEV) edge vortices can be clearly observed from these plots. The time instants of $t/T = 0$ and $t/T = 0.55$ approximately correspond to the instants of maximum LEV and TEV strengths, where T is the period of the lift cycle. Comparing the plots for the flap and baseline configurations, one observes that the vorticity within the LEV is of stronger magnitude for the flap case across all time instances. This result suggests that the flap dynamics are compatible with stronger LEV formation and an associated lower pressure that augments lift. At the same time, comparing the streamlines, we can observe that the flap is able to block the reverse flow associated with the TEV induced by flow separation. This blockage is particularly apparent in figures 10(b) and (c) versus figures 11(b) and (c), where the TEV is prominent. The figures indicate that these two mechanisms of enhanced LEV growth and reduced detrimental effects of TEV generation are the primary contributors to improved lift via the flap. Compatible

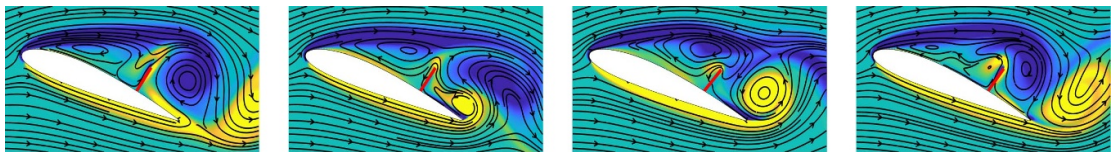

(a) $t = 0\ T$ (b) $t = 0.27\ T$ (c) $t = 0.55\ T$ (d) $t = 0.81\ T$

Figure 10. Vorticity contours at different time instants in one period of lift cycle for the case of flap hinge located at 70% of the chord length from the leading edge, $k_\beta = 0.001$ and $i_\beta = 0.0012$.

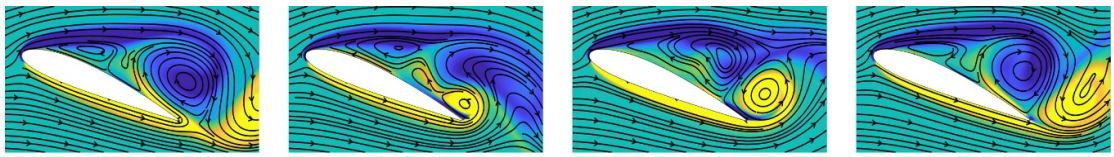

(a) $t = 0\ T$ (b) $t = 0.27\ T$ (c) $t = 0.55\ T$ (d) $t = 0.81\ T$

Figure 11. Vorticity contours at different time instants in one period of lift cycle for the flap-less case.

results were found in a separate set of flow simulations at the same low Reynolds number absent gravity in Nair and Goza [22], where the flap parameters induced an exchange between flap dynamics and the formation of the LEV and TEV.

While we do not present flow visualization data for $\mathrm{Re} = 200,000$, we expect important differences compared to $\mathrm{Re} = 1,000$, including fine-scale flow behavior and its effect on larger-scale behavior due to turbulence as well as distinct shedding dynamics consistent with leading and trailing edge separation locations that are different across Reynolds numbers due to differences in flow momentum relative to the imposed pressure gradient from the bluff body. That said, the fact that the flap-flow system preserves the dominant frequency behavior of the flap-less case for both Reynolds numbers suggests that similar mechanisms to those highlighted for the low Reynolds number might be relevant at the higher Reynolds number. We leave a detailed assessment of such a hypothesis to a future study.

4. Conclusions

This article set out to answer three questions related to the aerodynamic benefits of covert-inspired flaps across Reynolds number regimes (Q1), the dependency of such benefits on the flap structural parameters (Q2), and the physical mechanisms that govern the fluid-structure interactions across Reynolds numbers (Q3).

Our results for the first question (Q1) indicate that the flaps improve lift across Reynolds numbers. The low inertia flaps induce the most significant lift improvements with $\Delta\overline{C}_l$ up to 12%, reported at both Reynolds numbers. Similarities in lift improvement across Reynolds numbers are observed for flap locations where the relative location of the flap with respect to the separation location is similar. For example, for the location closest to the leading edge, the flap at both Reynolds numbers can interact with the leading-edge vortex. In contrast, at intermediate flap locations, and given the separation point location dependence of Reynolds number, the flap mean deflection angle and the corresponding lift effects are different across Reynolds numbers.

For the second question (Q2), which aims to relate the effect of the flap structural parameters to the lift improvements, the time-averaged results indicate that the hinge stiffness can be used to tailor the flap's mean deflection angle, which governs the resulting lift improvements. However, the flap location affects the sensitivity of the mean deflection angle to the changes in the hinge stiffness. Moreover, the instantaneous lift results reveal that the flap inertia mainly controls the flap oscillation amplitudes, where the high inertia flap has low amplitude oscillations, implying a quasi-static deployment and the low inertia flap has higher amplitude oscillations, suggesting dynamic deployment behavior. The fact that the dynamic low inertia flap yields superior lift enhancements compared to the quasi-static high inertia flap suggests a prominent role for the flap dynamics in enhancing lift and that torsionally hinged flaps, that are more analogous to feathers, are more effective in improving lift compared to static or rigidly mounted flaps.

Given the flap deployment dynamics difference, we examined the lift signal's frequency response to answer the third question (Q3). We presented two distinct lift enhancement mechanisms for the high and low inertia flap. The results suggest that the high inertia flap improves lift by preventing the interaction between the flow structures upstream and downstream of the flap, resulting in a pressure dam effect, as previously observed for static flaps. In contrast, the low inertia flap improves lift through the synchrony

between the shedding dynamics and the flap motion. More specifically, for the low Reynolds number case, the low inertia flap dynamics lead to enhanced LEV growth and reduced detrimental effects of TEV.

The results of this study can inform the design of flow control devices for engineered vehicles and form new hypotheses for the role of covert feathers in bird flight. For engineered vehicles, covert-inspired flaps are effective at improving lift at post-stall conditions and for a wide range of Reynolds numbers, suggesting that they can be deployed on vehicles of different sizes or at various flight speeds associated with various flight missions. As for the role of covert feathers during bird flight, future studies can measure the stiffness and inertia of covert feathers at multiple locations on birds' wings and examine the covert feather deployment behavior and dynamics to examine whether birds exploit different lift-enhancing mechanisms during flight, as discovered in this study for the bioinspired devices.

Data availability statement

All data that support the findings of this study are included within the article (and any supplementary files).

Acknowledgments

The authors would like to acknowledge funding from the National Science Foundation (Award No. 2029028). Moreover, certain images in this publication have been obtained by the author(s) from the Pixabay website, where they were made available under the Pixabay License. To the extent that the law allows, IOP Publishing disclaims any liability that any person may suffer as a result of accessing, using, or forwarding the image(s). Any reuse rights should be checked and permission should be asked for, if necessary, from Pixabay and/or the copyright owner (as appropriate) before using or forwarding the image(s).

Conflict of interest

The authors declare no competing interests.

Appendix

While the main article focused on the effect of the covert-inspired flaps on the lift and lift dynamics, in this appendix section, we extend the discussion to include the time-averaged drag forces. More specifically, we discuss the effects of the flap location, inertia, and hinge stiffness on the time-averaged lift $\overline{C_l}$ and drag $\overline{C_d}$ coefficients as a function of the angle of attack for some representative cases at $\mathrm{Re} = 200,000$. Examining lift and drag together provides a more complete picture of the effect of the covert-inspired flaps on performance or, more specifically, aerodynamic efficiency.

Figure 12 shows the time-averaged lift versus angle of attack, time-averaged drag versus angle of attack, and the drag polar (i.e. the lift coefficient versus the drag coefficient) for selected flap configurations. These configurations were selected to highlight the effect of the flap's location, hinge stiffness, and flap inertia on the aerodynamic forces and aerodynamic efficiency. We divide our discussion of the figure into pre-stall and post-stall regime observations, as the covert-inspired flaps are mainly post-stall lift enhancement flow control devices.

Pre-stall Regime: At pre-stall angles of attack ($\alpha \leqslant 16$), the flap effect on the lift force is mainly governed by the flap's location. Flaps at the same location have similar lift, regardless of the hinge stiffness and flap inertia (cf figure 12(a)). For instance, the trailing edge flaps ($0.7c$) have a slight detrimental effect on lift at low angles of attack, but they have the same maximum $\overline{C_l}$ as the baseline airfoil. The lift determinant at low angles of attack is due to the flap's interaction with the trailing edge vortex and causing the attached boundary layer near the trailing edge to separate. Moreover, a slight pre-stall drag penalty is observed for the trailing edge flaps due to the increased wake deficit (figure 12(b)). On the other hand, leading edge flaps ($0.2c$) have no effect on $\overline{C_l}$ at low angles of attack; however, they result in an earlier stall onset and lower maximum $\overline{C_l}$ compared to the baseline. The deployments of the $0.2c$ flaps around $\alpha = 9^\circ - 10^\circ$ disrupts the leading edge suction peak, resulting in an early stall. This early stall behavior is also noticeable in figure 12(b), where a significant step increase in drag occurs around ($\alpha = 9^\circ - 10^\circ$) due to the early deployment of the 0.2c flap. Overall, at pre-stall, an airfoil with a covert-inspired flap is slightly less efficient than the flap-less baseline due to the slight loss of lift and drag penalty (figure 12(b)).

Post-stall Regime: At post-stall angles of attack ($\alpha > 16$), the stiffness and inertia effects become more pronounced. For a given location and hinge stiffness, the low inertia flaps improve lift more than the high inertia flaps, with a maximum $\Delta\overline{C_l}$ of 15% compared to 11% for the high inertia flap. The inertia mainly controls the flap dynamics as shown in figure 7, which in turn controls the lift dynamics as shown in figures 8 and 9. The stiffness also plays a significant role, where a stiffer flap improves lift more for the trailing edge location, while the less stiff flap performs better at the leading edge location. At post-stall, for most configurations, there are no drag penalties associated with the lift improvements (cf figure 12(b)). It is also noteworthy that some flap configurations improve lift and reduce drag by up to 12%. As a result, a significant enhancement in aerodynamic efficiency is noticed for the airfoil with the flap compared to the baseline post-stall (figure 12(c)).

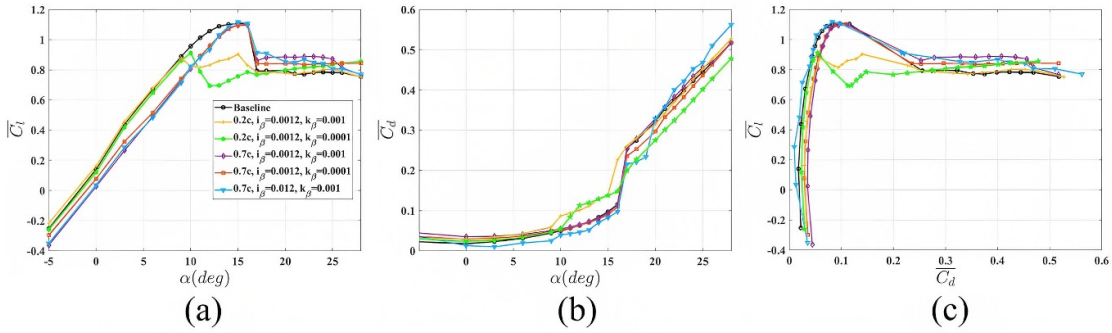

Figure 12. a) Experimental $\overline{C_l}$ versus α. (b) $\overline{C_d}$ versus α, and (c) $\overline{C_l}$ versus $\overline{C_d}$ plots for representative cases of varying location, stiffness, and inertia at Re $= 200,000$.

ORCID iDs

Ahmed K Othman https://orcid.org/0009-0002-1190-418X
Nirmal J Nair https://orcid.org/0000-0003-4431-4020
Andres Goza https://orcid.org/0000-0002-9372-7713
Aimy Wissa https://orcid.org/0000-0002-8468-511X

References

[1] Altman A and Allemand G 2016 Post-stall performance improvement through bio-inspired passive covert feathers *54th AIAA Aerospace Sciences Meeting* p 2042
[2] Apelt C J and West G S 1975 The effects of wake splitter plates on bluff-body flow in the range $10^4 < r < 5 \times 10^4$. Part 2 *J. Fluid Mech.* **71** 145–60
[3] Bachmann T, Emmerlich J, Baumgartner W, Schneider J M and Wagner H 2012 Flexural stiffness of feather shafts: geometry rules over material properties *J. Exp. Biol.* **215** 405–15
[4] Barlow J B, Rae W H and Pope A 1999 *Low-Speed Wind Tunnel Testing* (Wiley)
[5] Singh Batth R *et al* 2020 Classification of unmanned aerial vehicles: a mirror review *2020 Int. Conf. on Intelligent Engineering and Management (ICIEM)* (IEEE) pp 408–13
[6] Bechert D, Bruse M, Hage W, Meyer R, Bechert D, Bruse M, Hage W and Meyer R 1997 Biological surfaces and their technological application-laboratory and flight experiments on drag reduction and separation control *28th Fluid Dynamics Conf.* p 1960
[7] Brown R E and Roger Fedde M 1993 Airflow sensors in the avian wing *J. Exp. Biol.* **179** 13–30
[8] Brücker C and Weidner C 2014 Influence of self-adaptive hairy flaps on the stall delay of an airfoil in ramp-up motion *J. Fluids Struct.* **47** 31–40
[9] Carruthers A C, Thomas A L R and Taylor G K 2007 Automatic aeroelastic devices in the wings of a steppe eagle aquila nipalensis *J. Exp. Biol.* **210** 4136–49
[10] Colonius T and Taira K 2008 A fast immersed boundary method using a nullspace approach and multi-domain far-field boundary conditions *Comput. Methods Appl. Mech. Eng.* **197** 2131–46
[11] Duan C and Wissa A 2021 Covert-inspired flaps for lift enhancement and stall mitigation *Bioinspir. Biomim.* **16** 046020
[12] Evers J H 2007 Biological inspiration for agile autonomous air vehicles *Platform Innovations and System Integration for Unmanned Air, Land and Sea Vehicles (AVT-SCI Joint Symp.)* pp 1–14
[13] Fahlstrom P G, Gleason T J and Sadraey M H 2022 *Introduction to UAV Systems* (Wiley)
[14] Gad-el Hak M 2000 *Flow Control: Passive, Active and Reactive Flow Management* (Cambridge University Press)
[15] Gad-el Hak M, Pollard A and Bonnet J-P 2003 *Flow Control: Fundamentals and Practices* vol 53 (Springer)
[16] Giguère P and Selig M S 1997 Freestream velocity corrections for two-dimensional testing with splitter plates *AIAA J.* **35** 1195–200
[17] Goza A and Colonius T 2017 A strongly-coupled immersed-boundary formulation for thin elastic structures *J. Comput. Phys.* **336** 401–11
[18] Goza A, Colonius T and Sader J E 2018 Global modes and nonlinear analysis of inverted-flag flapping *J. Fluid Mech.* **857** 312–44
[19] Johnston J and Gopalarathnam A 2012 Investigation of a bio-inspired lift-enhancing effector on a 2D airfoil *Bioinspir. Biomim.* **7** 036003
[20] Meyer R, Hage W, Bechert D W, Schatz M, Knacke T and Thiele F 2007 Separation control by self-activated movable flaps *AIAA J.* **45** 191–9
[21] Nair N J and Goza A 2022 A strongly coupled immersed boundary method for fluid-structure interaction that mimics the efficiency of stationary body methods *J. Comput. Phys.* **454** 110897
[22] Nair N J and Goza A 2022 Fluid-structure interaction of a bio-inspired passively deployable flap for lift enhancement *Phys. Rev. Fluids* **7** 064701
[23] Nair N J, Flynn Z and Goza A 2022 Numerical study of multiple bio-inspired torsionally hinged flaps for passive flow control *Fluids* **7** 44
[24] Othman A K, Nair N J, Sandeep A, Goza A and Wissa A 2022 Numerical and experimental study of a covert-inspired passively deployable flap for aerodynamic lift enhancement *AIAA AVIATION 2022 Forum*
[25] Othman A K, Zekry D A, Saro-Cortes V, Lee K J P and Wissa A A 2023 Aerial and aquatic biological and bioinspired flow control strategies *Commun. Eng.* **2** 30
[26] Pixabay/TheOtherKev 2021 (available at: https://pixabay.com/photos/heron-in-flight-blue-heron-heron-4158846/)
[27] Roshko A 1961 Experiments on the flow past a circular cylinder at very high reynolds number *J. Fluid Mech.* **10** 345–56
[28] Rosti M E, Omidyeganeh M and Pinelli A 2018 Passive control of the flow around unsteady aerofoils using a self-activated deployable flap *J. Turbulence* **19** 204–28

[29] Selig M, Broeren A P and Giguère P 1995 *Summary of low-Speed Airfoil Data : low-Speed Airfoil Test* (*University of Illinois at Urbana-Champaign*) (SoarTech)
[30] U.S. Fish & Wildlife Service/The Feather Atlas 2021 (available at: www.fws.gov/lab/featheratlas/feather.php?Bird = GBHE_covert_imm)
[31] Wang L, Mahbub Alam Md and Zhou Y 2019 Experimental study of a passive control of airfoil lift using bioinspired feather flap *Bioinspir. Biomim.* **14** 066005
[32] Wang X, Nudds R L, Palmer C and Dyke G J 2012 Size scaling and stiffness of avian primary feathers: implications for the flight of mesozoic birds *J. Evol. Biol.* **25** 547–55